RESEARCH ARTICLE

Key Points:
- A traveling convection vortex (TCV) event was observed in association with transient phenomena in the solar wind
- Ionospheric convection changes, auroral precipitation, enhancements in plasma density and temperature, and wave activity were observed
- A divergence in thermospheric winds associated with the TCV, due to thermospheric heating, was also measured

Correspondence to:
H. Kim,
hmkim@njit.edu

Simultaneous observations of traveling convection vortices: Ionosphere-thermosphere coupling

Hyomin Kim[1] [ID], **Marc R. Lessard[2], Sarah L. Jones[3], Kristina A. Lynch[4], Philip A. Fernandes[5]** [ID], **Anasuya L. Aruliah[6], Mark J. Engebretson[7]** [ID], **Jøran I. Moen[8,9], Kjellmar Oksavik[9,10]** [ID], **Alexander G. Yahnin[11]**, and **Timothy K. Yeoman[12]** [ID]

[1]Center for Solar-Terrestrial Research, New Jersey Institute of Technology, Newark, New Jersey, USA, [2]Space Science Center, University of New Hampshire, Durham, New Hampshire, USA, [3]Space Weather Laboratory, NASA Goddard Space Flight Center, Greenbelt, Maryland, USA, [4]Department of Physics and Astronomy, Dartmouth College, Hanover, New Hampshire, USA, [5]ISR-1 Space Science and Applications, Los Alamos National Laboratory, Los Alamos, New Mexico, USA, [6]Department of Physics and Astronomy, University College London, London, UK, [7]Department of Physics, Augsburg College, Minneapolis, Minnesota, USA, [8]Department of Physics, University of Oslo, Oslo, Norway, [9]University Centre in Svalbard, Longyearbyen, Norway, [10]Birkeland Centre for Space Science, Department of Physics and Technology, University of Bergen, Bergen, Norway, [11]Polar Geophysical Institute, Apatity, Russia, [12]Department of Physics and Astronomy, University of Leicester, Leicester, UK

Abstract We present simultaneous observations of magnetosphere-ionosphere-thermosphere coupling over Svalbard during a traveling convection vortex (TCV) event. Various spaceborne and ground-based instruments made coordinated measurements, including magnetometers, particle detectors, an all-sky camera, European Incoherent Scatter (EISCAT) Svalbard Radar, Super Dual Auroral Radar Network (SuperDARN), and SCANning Doppler Imager (SCANDI). The instruments recorded TCVs associated with a sudden change in solar wind dynamic pressure. The data display typical features of TCVs including vortical ionospheric convection patterns seen by the ground magnetometers and SuperDARN radars and auroral precipitation near the cusp observed by the all-sky camera. Simultaneously, electron and ion temperature enhancements with corresponding density increase from soft precipitation are also observed by the EISCAT Svalbard Radar. The ground magnetometers also detected electromagnetic ion cyclotron waves at the approximate time of the TCV arrival. This implies that they were generated by a temperature anisotropy resulting from a compression on the dayside magnetosphere. SCANDI data show a divergence in thermospheric winds during the TCVs, presumably due to thermospheric heating associated with the current closure linked to a field-aligned current system generated by the TCVs. We conclude that solar wind pressure impulse-related transient phenomena can affect even the upper atmospheric dynamics via current systems established by a magnetosphere-ionosphere-thermosphere coupling process.

1. Introduction

Sudden changes in the solar wind (e.g., interplanetary magnetic field (IMF) or flow velocity) are manifested in various forms in the ionosphere. Magnetic impulse events (MIEs) [e.g., *Araki*, 1977] or traveling convection vortices (TCVs) [e.g., *Friis-Christensen et al.*, 1988; *Glassmeier et al.*, 1989] are typically seen in high-latitude magnetic field data during such transient events, displaying sudden bipolar deflections in the fields (several hundreds of nanotesla). TCVs, a particular type of MIEs, are characterized by a series of vortices representing $\mathbf{E} \times \mathbf{B}$ convection propagating longitudinally from the dayside to nightside at the speed of ∼3–10 km/s with a duration of a few minutes to half an hour. The approximate horizontal size of the vortices ranges between 1000 and 3000 km, and the vortex center (corresponding to the maximum deflection) typically appears at ∼73–75° magnetic latitudes (MLATs) [*Friis-Christensen et al.*, 1988; *Glassmeier et al.*, 1989; *Glassmeier and Heppner*, 1992; *Yahnin et al.*, 1995, 1997; *Moretto and Yahnin*, 1998; *Zesta et al.*, 1999; *Amm et al.*, 2002; *Moretto et al.*, 2002; *Murr et al.*, 2002; *Zesta et al.*, 2002; *Fillingim et al.*, 2011]. The vortical structure in ionospheric convection is due to Hall currents generated by field-aligned currents (FACs) associated with the transient response near/at the magnetopause. The longitudinal propagation of TCVs is attributed to azimuthal plasma flow motion along the magnetopause associated with solar wind transient changes [*McHenry and Clauer*, 1987; *Friis-Christensen et al.*, 1988; *Glassmeier et al.*, 1989; *Kivelson and Southwood*, 1991; *Sibeck et al.*, 2003].

Table 1. Geographic and Geomagnetic Locations of International Monitor for Auroral Geomagnetic Effects (IMAGE) and Greenland Fluxgate Magnetometers[a]

| Site Location	Geographic		CGM		UT of
	Latitude (N)	Longitude (E)	Latitude (N)	Longitude (E)	0000 MLT
Ny-Ålesund (NAL)	78.92	11.95	76.41	109.59	2106
Longyearbyen (LYR)	78.20	15.82	75.47	110.63	2112
Hornsund (HOR)	77.00	15.60	74.34	108.24	2110
Hopen Island (HOP)	76.51	25.01	73.32	114.04	2046
Bear Island (BJN)	74.50	19.20	71.64	106.98	2113
Nordkapp (NOR)	71.09	25.79	67.93	108.65	2105
Kevo (KEV)	69.76	27.01	66.54	108.59	2105
Godhavn (GDH)	69.25	306.47	75.05	38.45	0233
Lovozero (LOZ)	67.97	35.02	64.49	114.00	2041

[a]The University of New Hampshire (UNH) induction-coil magnetometers are located at Ny-Ålesund (NAL), Longyearbyen (LYR), and Hornsund (HOR) on Svalbard. Data from the Polar Geophysical Institute induction-coil magnetometer in Lovozero (LOZ), Russia, are also used. The geomagnetic coordinates of the stations are obtained from the International Geomagnetic Reference Field (IGRF) Corrected Geomagnetic (CGM) model for Epoch 2010.

Several TCV generation mechanisms have been suggested: for example, flux transfer events [*Goertz et al.*, 1985; *Lanzerotti et al.*, 1987], solar wind dynamic pressure impulse interactions with the magnetopause [*Friis-Christensen et al.*, 1988; *Glassmeier and Heppner*, 1992; *Sibeck et al.*, 1989, 2003; *Araki*, 1994; *Kim et al.*, 2015; *Tian et al.*, 2016], and Kelvin-Helmholtz instabilities [*McHenry et al.*, 1990; *Clauer and Ridley*, 1995; *Clauer and Petrov*, 2002; *Clauer*, 2003; *Dougal et al.*, 2013]. It is now generally accepted that TCVs are caused by pressure perturbations due to solar wind buffeting of the magnetosphere. A number of observations [e.g., *Sitar et al.*, 1998; *Zesta et al.*, 1999; *Sibeck et al.*, 2003; *Kim et al.*, 2015] and theoretical models [e.g., *Kivelson and Southwood*, 1991] showed that solar wind pressure impulse events are the major cause of TCVs. Some studies [e.g., *Murr and Hughes*, 2003; *Kataoka et al.*, 2003, 2004] found that nearly all of the events they studied were excited by disturbances born in the solar wind just upstream of the bow shock (i.e., ion foreshock). Refer to *Kim et al.* [2015] for further information about TCVs.

It has been reported that magnetospheric compression causes generation of electromagnetic ion cyclotron (EMIC) waves due to increased proton temperature anisotropies in the magnetosphere [e.g., *Anderson et al.*, 1992; *Usanova et al.*, 2012]. TCV-associated Pc1 pulsations (interpreted as EMIC waves) have been observed on the ground [e.g., *Posch et al.*, 2013; *Engebretson et al.*, 2013]. Dynamics associated with ionospheric plasma during TCV events have also been reported. Observations using the European Incoherent Scatter (EISCAT) and Sondrestrom radars show significant plasma density erosion due to recombination of oxygen caused by increased frictional heating (T_i) within the vortex [*Valladares et al.*, 1999]. *Lühr et al.* [1996] used EISCAT to measure the conductivity associated with the vortices and found increased conductivity in the downward field-aligned current region. Super Dual Auroral Radar Network (SuperDARN) data show enhancement and motion of ionospheric flow in association with TCVs [e.g., *Engebretson et al.*, 2013].

Studies have reported ionosphere-thermosphere coupling processes, showing that the high-latitude thermospheric dynamics are controlled by the solar wind and magnetospheric and ionospheric activities (e.g., Joule heating and electron precipitation) [e.g., *Aruliah et al.*, 1991; *Aruliah and Griffin*, 2001; *Thayer and Semeter*, 2004; *Wang et al.*, 2004; *Wiltberger et al.*, 2004, and references therein]. The solar wind controls FACs and plasma flows in the ionosphere, and neutral air density in the thermosphere, depositing significant energy in the cusp region from the magnetosphere into the ionosphere/thermosphere [*Wang et al.*, 2014]. Some studies [e.g., *Lanchester et al.*, 2001; *Otto et al.*, 2003; *Lühr et al.*, 2004] have suggested that small-scale FACs play an important role in thermospheric heating.

This paper presents simultaneous observations of magnetosphere-ionosphere-thermosphere coupling during a TCV event in association with transient phenomena in the solar wind, which is perhaps, to the best of the authors' knowledge, the first report of observations showing ionosphere-thermosphere coupling in conjunction with a TCV event. During the Rocket Experiment for Neutral Upwelling (RENU) launch campaign
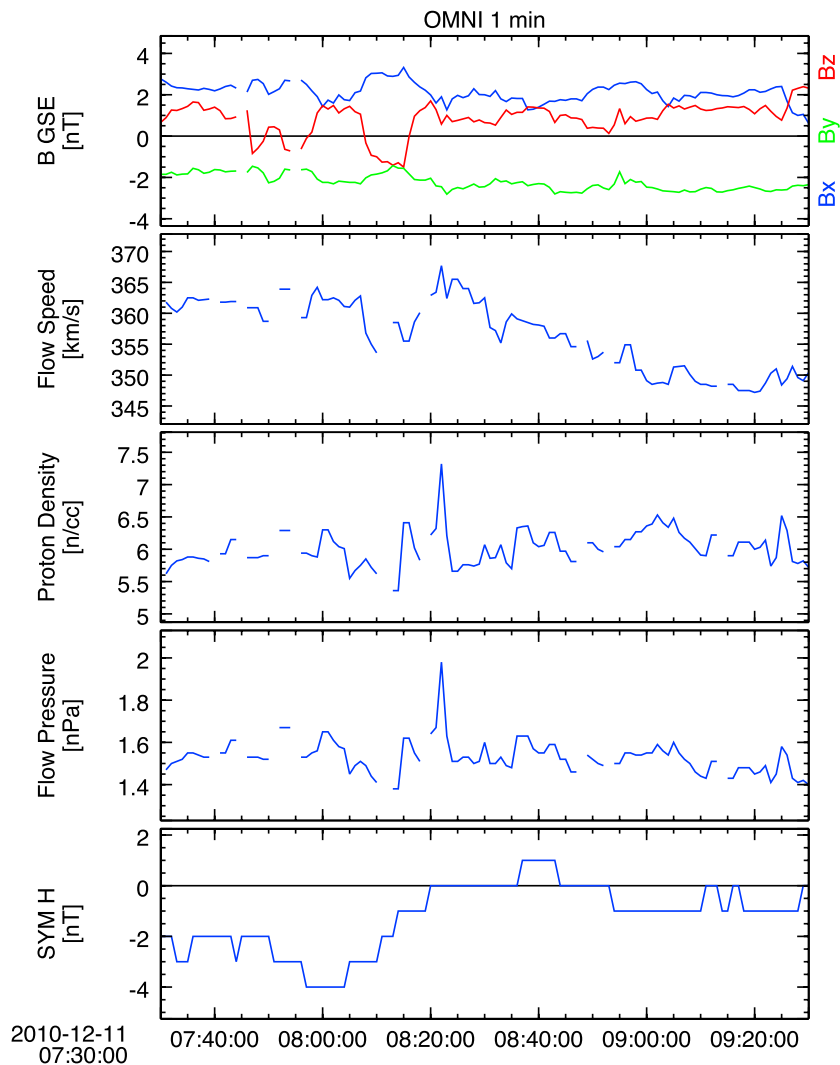
Figure 1. High time resolution (1 min) OMNI 1 AU data showing IMF B_z northward turning and solar wind dynamic pressure impulse at ~08:15 UT. The Space Physics Environment Data Analysis Software (SPEDAS) tool was used to plot the OMNI data obtained from the OMNI database (http://omniweb.gsfc.nasa.gov).

in late 2010, the science team spent several weeks in Longyearbyen on Svalbard observing the ionosphere in support of the launch call. During this time, various ground-based instruments made coordinated measurements, including magnetometers, an all-sky camera, EISCAT Svalbard Radar, SuperDARN, and SCANning Doppler Imager (SCANDI) near the launch site. On 11 December 2010, the instruments recorded TCVs associated with a sudden change in solar wind dynamic pressure. We present data showing ionospheric convection patterns observed by the ground magnetometers and a corresponding divergence of thermospheric winds observed by SCANDI as well as EMIC wave observations from the ground beneath the event as it transited overhead. These include the first-ever observations of thermospheric heating associated with TCVs.

2. Data Set

High-resolution (1 min) OMNI data time shifted to the nose of the Earth's bow shock (J. H. King and N. Papitashvilli, P.I.) were used for investigation of solar wind conditions. The OMNI data are processed from magnetic field and plasma measurements recorded by the Advanced Composition Explorer, Wind, Interplanetary Monitoring Platform-8, and Geotail spacecraft.

Fluxgate magnetometer data were obtained by the International Monitor for Auroral Geomagnetic Effects (IMAGE) and Technical University of Denmark (DTU) Greenland network providing 10 s and 1 s (time stamped
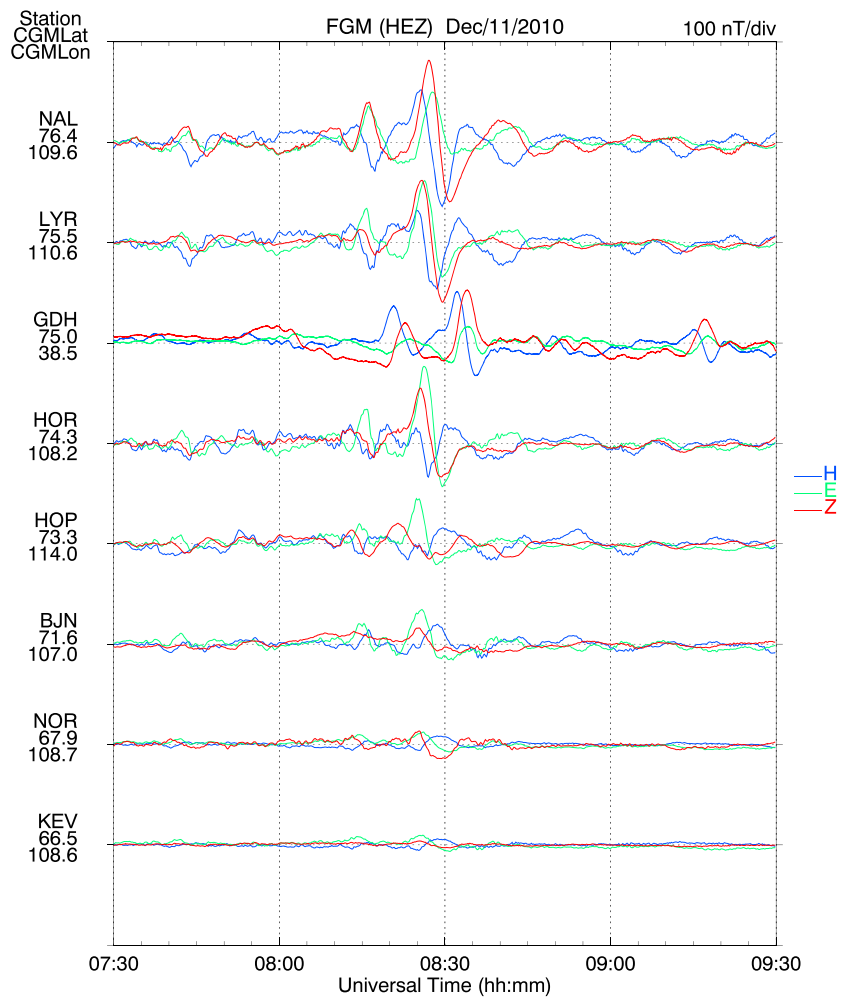
Figure 2. Magnetometer data from the IMAGE and Greenland magnetometer network, showing the passage of the TCV starting at ~08:20 UT.

for the beginning of the 10 s interval) time resolution data, respectively. The IMAGE and Greenland magnetic field data used in this study are represented in the *HEZ* coordinate system, in which *H* is toward the local geomagnetic north in the horizontal plane, *Z* downward toward the Earth, and *E* completes the right-hand rule pointing eastward. The locations of the magnetometers used in this study are listed in Table 1. Magnetic field pulsations in the ultralow frequency (ULF) are monitored by the three University of New Hampshire's (UNH) induction-coil magnetometers located on Svalbard, Norway (Ny-Ålesund (NAL), Longyearbyen (LYR), and Hornsund (HOR)) and the Polar Geophysical Institute induction-coil magnetometer in Lovozero (LOZ), Russia (also see Table 1). The induction-coil magnetometers provide two-axis time-varying magnetic field (dB/dt) measurements in local geomagnetic coordinates with *X* northward and *Y* eastward at the rate of 10 samples/s (NAL, LYR, and HOR) and 40 samples/s (LOZ).

Particle data from the Medium Energy Proton and Electron Detector (MEPED) aboard the low Earth-orbiting (~800 km in altitude) National Oceanic and Atmospheric Administration (NOAA) and MetOp spacecraft are used to examine electron and ion precipitation. This instrument includes a set of solid-state energetic particle detectors that monitor the intensities of protons and electrons over a range extending from 30 keV to more than 200 MeV. The MEPED instrument has two detectors. Both point upward at angles of 10° and 80° with a vector from the Earth center to the spacecraft. At high latitudes, the 10° telescope measures particles within the loss cone (i.e., precipitating flux) and 80° telescope measures particles outside the loss cone (i.e., trapped particles). The Special Sensor J instrument aboard the Defense Meteorological Satellite Program (DMSP) satellite is also used for observations of precipitating electrons and ions at an altitude of ~850 km over a range of energies from 30 eV to 30 keV.
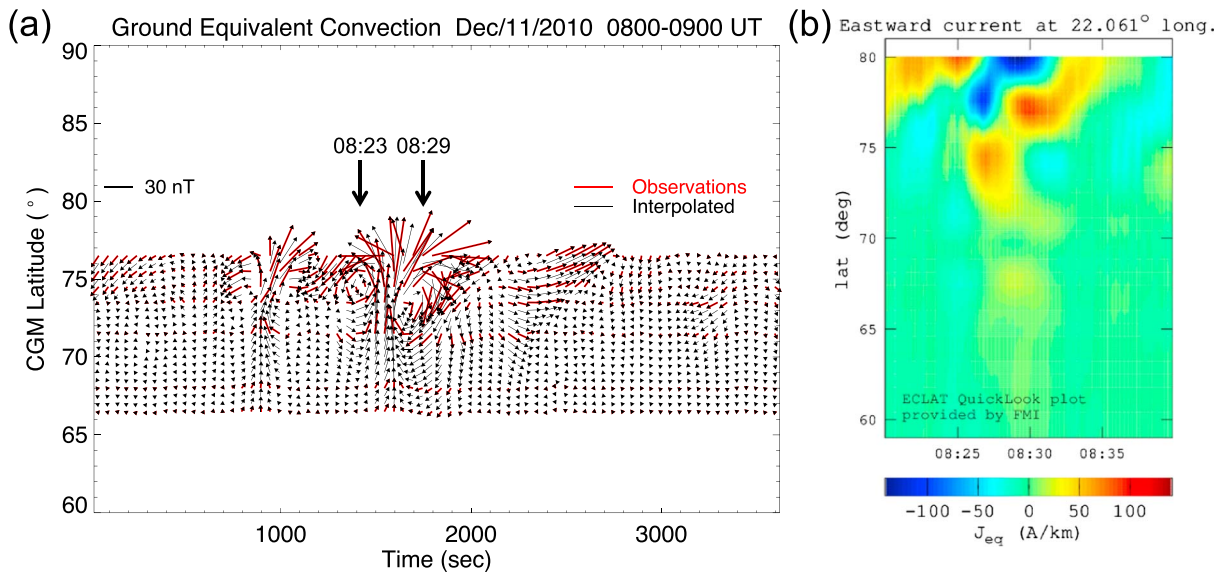
Figure 3. Ground equivalent convection (a) vectors and (b) currents inferred from the magnetic field data shown in Figure 2. Latitudinally interpolated convection vectors are displayed in black lines overplotted with the observed convection patterns in red lines. The centers of each convection vortex are indicated by the arrows at 08:23 and 08:29 UT, respectively. The 2-D equivalent current plot is generated by the online tool provided by the IMAGE Network website at http://space.fmi.fi/MIRACLE/iono_2D.php. Note that the latitudes in Figure 3b are geographic.

To examine auroral activity, images from the University of Oslo all-sky camera in LYR are presented. These images are obtained at 630.0 nm every 30 s. The images are projected onto the world map using an assumed emission altitude of 250 km for the 630.0 nm emissions.

Ionospheric disturbances (e.g., variations in plasma convection and temperature) are measured by the EISCAT Svalbard and SuperDARN radars. Field-of-view (FOV) ionospheric convection velocity (2 min averaged) maps are provided by data from the SuperDARN radar covering the region of interest in this study. The radar is located at Hankasalmi, Finland (62.32°N, 26.61°E, geographic). The EISCAT Svalbard Radar is located in LYR (78.153°N, 16.029°E). In this paper we present EISCAT data from the 42 m dish antenna, which is fixed in a direction parallel with the local magnetic field (81.6° elevation, 184.5° azimuth). On 11 December 2010 the EISCAT Svalbard Radar operated in an experiment mode that gave vertical profiles of the electron density, the electron and ion temperatures, and the ion drift velocity in the vertical direction.

Thermospheric wind and neutral temperature measurements at 8 min resolution are provided by the wide-field Fabry-Perot Interferometer (FPI) called SCANDI [*Aruliah et al.*, 2010]. This has an outer zenith angle of 67°, which gives an FOV radius of 589 km for an atomic oxygen red line (630.0 nm) emission, assuming that it peaks at 250 km altitude. The range observed is about 10° latitude centered at LYR. The image exposure time is 7–8 min, including time to process the photon counts.

3. Observations

In this section, we present coordinated observations of a TCV event during the RENU campaign at Longyearbyen, Svalbard, in late 2010. The event was observed on 11 December 2010 by all ground-based instruments listed in the previous section. Shown here are a series of data sets supporting the occurrence of the TCV event associated with a transient change in solar wind dynamic pressure and auroral particle precipitation. These phenomena coincided with ionospheric convection and temperature changes. In addition to the well-coordinated observations of magnetosphere-ionosphere coupling associated with the TCV event, we show a thermospheric neutral wind divergence, which might be the first evidence of thermospheric coupling with the ionospheric convection phenomena generated by FACs in conjunction with the transient event.

The OMNI data in Figure 1 present solar wind conditions from 07:30 to 09:30 UT on 11 December 2010. The most remarkable feature in the OMNI data is the solar wind dynamic pressure impulse that occurred approximately at 08:15 UT (fourth panel), increasing the pressure from 1.4 to 2 nPa in 7 min. The IMF data (top panel)
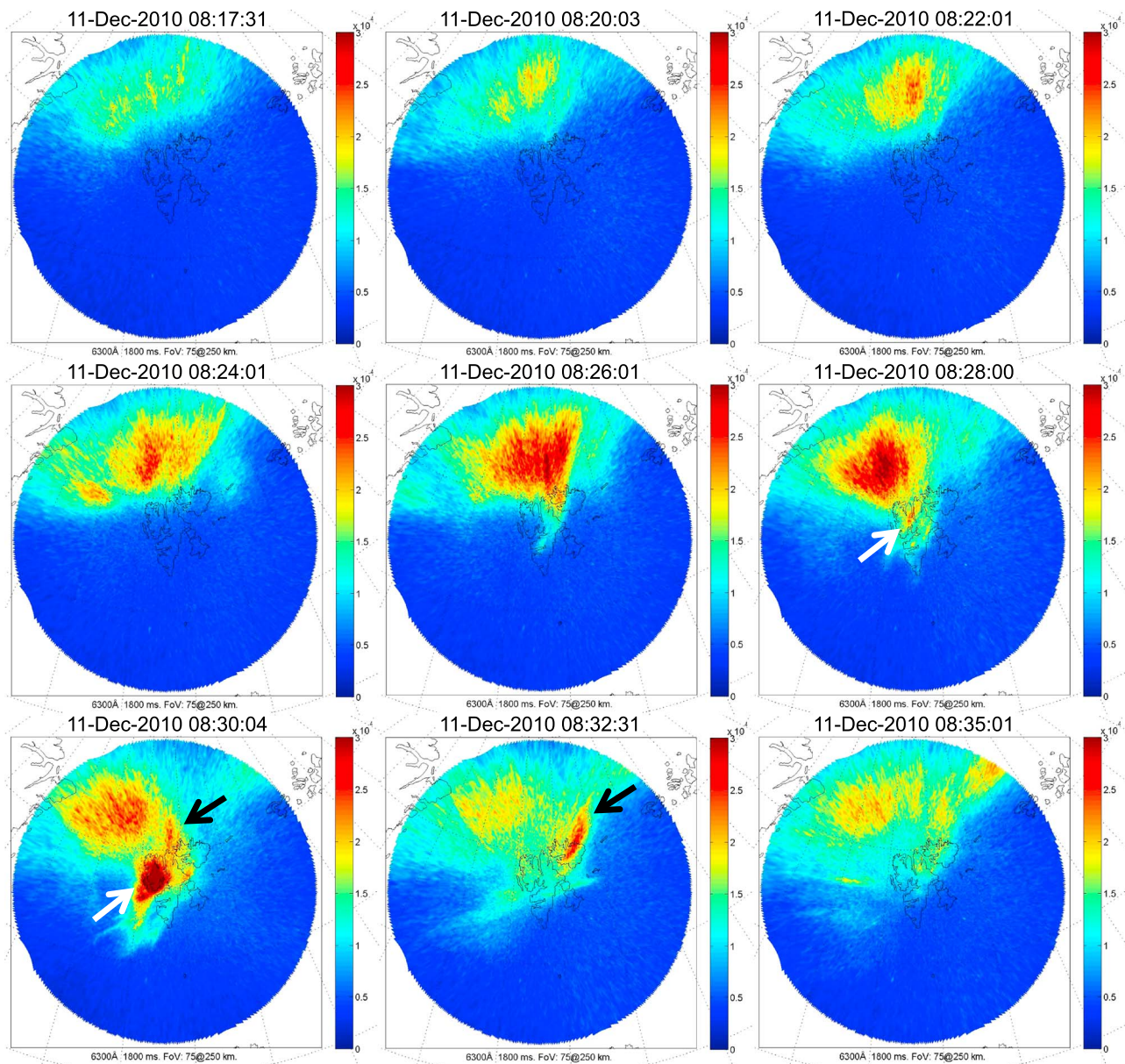
Figure 4. University of Oslo all-sky camera images from LYR at 630.0 nm acquired during the TCV event. The emissions occurring poleward of the station before the event are thought to be cusp precipitation. The emissions associated with the TCVs are the brief, bright spots directly over LYR.

show a northward turning of the field during this event. The $SYM - H$ index indicates very quiet geomagnetic activity. Also, note that the Kp index was 0 during this period.

Figure 2 presents time series plots of IMAGE and Greenland magnetometer data. The top part shows data from the geomagnetically northernmost station and the bottom part the southernmost. The station codes and their corrected geomagnetic (CGM) coordinates are labeled at the left of each panel. The magnetic field traces in this figure are baseline subtracted to isolate TCV structures from the background. The latitudinally spaced magnetometers display typical features of TCVs (e.g., bipolar deflections in the fields) starting at ~08:20 UT (~11:20 in magnetic local time (MLT)). The maximum deflection is seen at NAL located at 76.5° MLAT. The TCV event occurred simultaneously with the solar wind pressure impulse shown in the OMNI data (see Figure 1).

Also shown in Figure 2 are data from Godhavn (GDH) in Greenland, located at a similar geomagnetic latitude to that of LYR and separated by 72° in longitude from LYR (~2200 km geographically). A cross-correlation
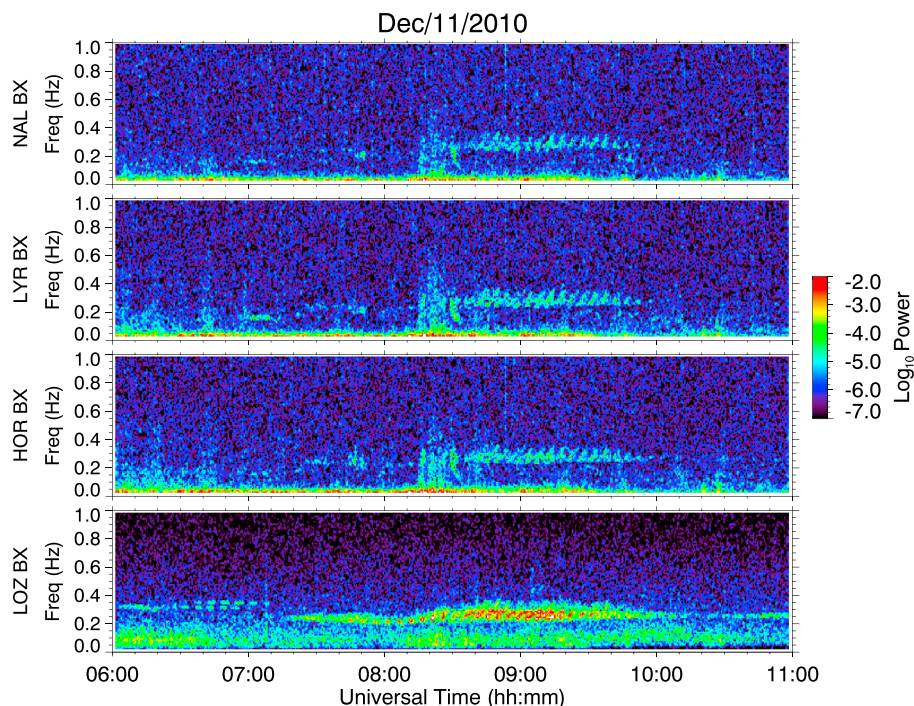
Figure 5. Fast Fourier transform (FFT) spectrograms showing EMIC waves observed at NAL, LYR, HOR, and LOZ in conjunction with the TCVs which occurred between ∼08:20 UT and 08:30 UT.

analysis for the TCV signatures between the longitudinally spaced stations, LYR and GDH, reveals that the TCV event at GDH is lagged by 452 s with the cross-correlation coefficient of 0.5. This result indicates that the event propagated westward (away from local noon) at the speed of ∼4.9 km/s, which is within the typical range of TCV propagation speed as observed in the aforementioned studies. Typically, signals from longitudinally
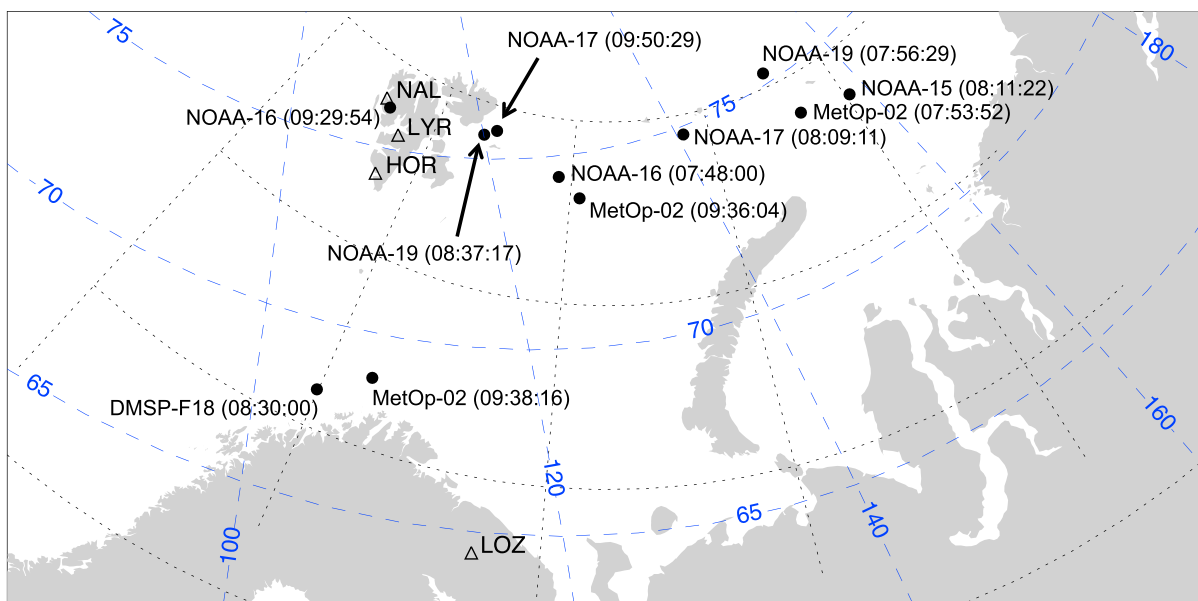
Figure 6. Map showing the locations of induction-coil magnetometer stations (triangles) and geomagnetic footprints of low Earth orbit spacecraft that observed medium energy (30–80 keV) proton precipitation (closed circles). The universal times when each spacecraft measured the maximum fluxes during the overflight near Svalbard are shown in the parenthesis next to each spacecraft name. The position of NOAA 19 at 07:56:29 UT is a geomagnetic footprint in the Northern Hemisphere projected from its orbit coordinates in the Southern Hemisphere. The black dotted lines and blue dashed lines represent geographic and (IGRF based) geomagnetic latitudes and longitudes, respectively.
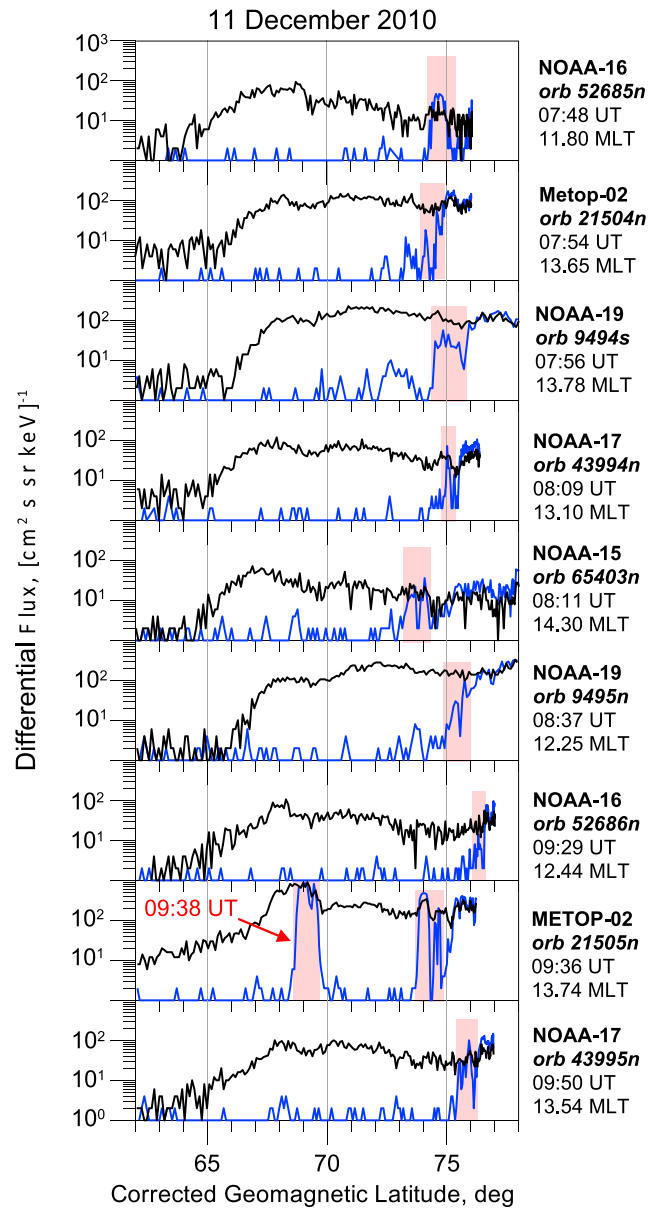
Figure 7. Medium energy (30–80 keV) proton flux from the MEPED instrument aboard the NOAA and MetOp spacecraft during the flight near Svalbard on 11 December 2010. The black and blue traces indicate trapped and precipitating flux, respectively. The proton precipitation that occurred within the anisotropic zone is marked by pink color. Times (UT and MLT) when each spacecraft measured the maximum fluxes are labeled at the right of each panel (cf. Figure 6).

spaced stations are compared to infer the propagation direction and speed of TCVs. Combining this result with the following observations (as shown in Figures 3 and 10 in particular), we confirm that the event is TCVs.

Ionospheric convection flow motion ($\mathbf{E} \times \mathbf{B}$) associated with the TCV event is inferred from the ground magnetometer data as presented in Figure 3. The convection patterns are obtained by rotating the horizontal magnetic fields averaged over 50 s interval by 90° counterclockwise after removing the baselines of the data. The approximate size of the vortices is seen from the latitudinally stacked temporal changes of the flow motion. The latitudinal spaces between distant stations are filled with interpolated vectors, and thus, the patterns are more clearly seen. This interpolation was performed based on an assumption that the ionospheric conductivity is uniform over the area of observations (Svalbard and northern Norway) because the event in this study occurred under dark conditions (December). Of course, this assumption may not hold due to local conductivity change caused by auroral precipitation. The nonuniform conductivity may result in rather
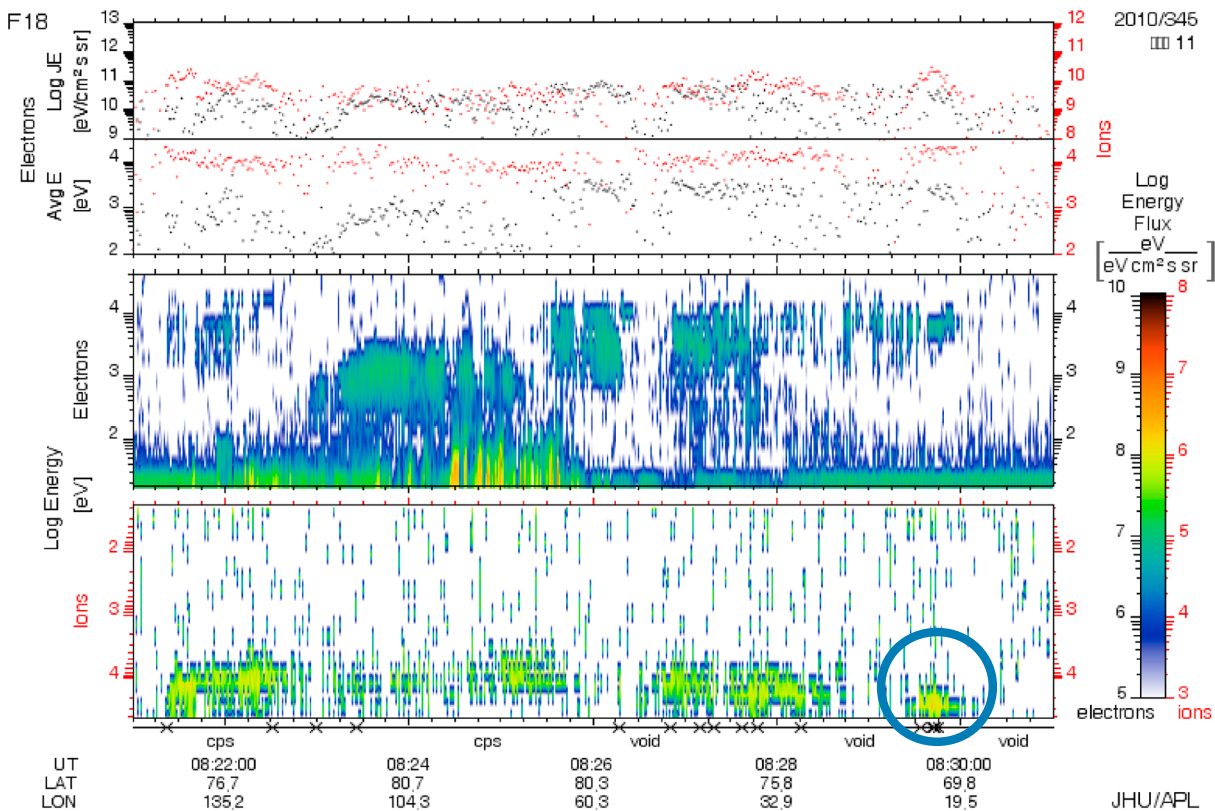
Figure 8. Spectrograms of electron and ion flux data from DMSP-F18. (top to bottom) Particle flux intensities of electrons and ions, average energy of the particles, and spectrograms for electrons and ions. The precipitation regions and boundaries are marked at the bottom. Encircled is the proton burst of interest, which is a useful source marker for the EMIC wave event.

distorted convection patterns. However, we note that this technique is to identify the approximate spatial extent of TCV events, which may not be significantly affected by the local conductivity change. This technique has been widely used in a number of studies [e.g., *Friis-Christensen et al.*, 1988; *Glassmeier et al.*, 1989; *Yahnin et al.*, 1995; *Sitar et al.*, 1998; *Engebretson et al.*, 2013; *Kim et al.*, 2015]. Figure 3b displays ground equivalent convection currents also inferred from the IMAGE magnetic field data shown in Figure 2. A twin vortex, whose centers are located at ~73°–74° MLAT, is clearly seen between approximately 08:20 and 08:35 UT as shown in Figure 3a. The centers of each convection vortex are indicated by the arrows at 08:23 and 08:29 UT, respectively. Eastward (+) and westward (−) currents corresponding to the TCVs are also seen in Figure 3b.

Figure 4 presents all-sky camera images filtered at 630 nm, which were acquired at LYR during the TCVs. The emissions occurring poleward of the station before the event are thought to be cusp precipitation. This cusp aurora brightens over the period from 8:22 UT to 8:28 UT, at which point the emissions begin to extend southward over the northeastern island of the Svalbard archipelago and weakly over the rest of Svalbard. Within the FOV of the all-sky camera the bulk of the cusp emissions drifts westward, including the bright spot that had appeared over the northeastern island. At 8:28 UT there is a patch of emissions roughly over NAL that brightens and remains fixed until disappearing at ~8:32 UT (see the white arrows). Simultaneously, a small patch appears in the image at ~8:30 UT over the northern island (see the black arrows). This small patch drifts northeastward, brightens and expands, and appears to merge back into the main region of cusp precipitation by approximately 8:34 UT. These brief, bright spots over Svalbard are thought to be directly related to the passing of the TCVs because the convection centers (as shown in Figure 3) coincide with the spatial and temporal extent of the auroral precipitation.

Figure 5 shows fast Fourier transform (FFT) spectrograms of data from the three induction-coil magnetometers on Svalbard (NAL, LYR, and HOR) and one induction-coil magnetometer in Russia (LOZ). Magnetic field pulsations in the ULF Pc1 range (0.2–5 Hz) are clearly seen in the spectrograms. Pc1–2 pulsations are generally considered to be electromagnetic ion cyclotron (EMIC) waves associated with increased proton temperature
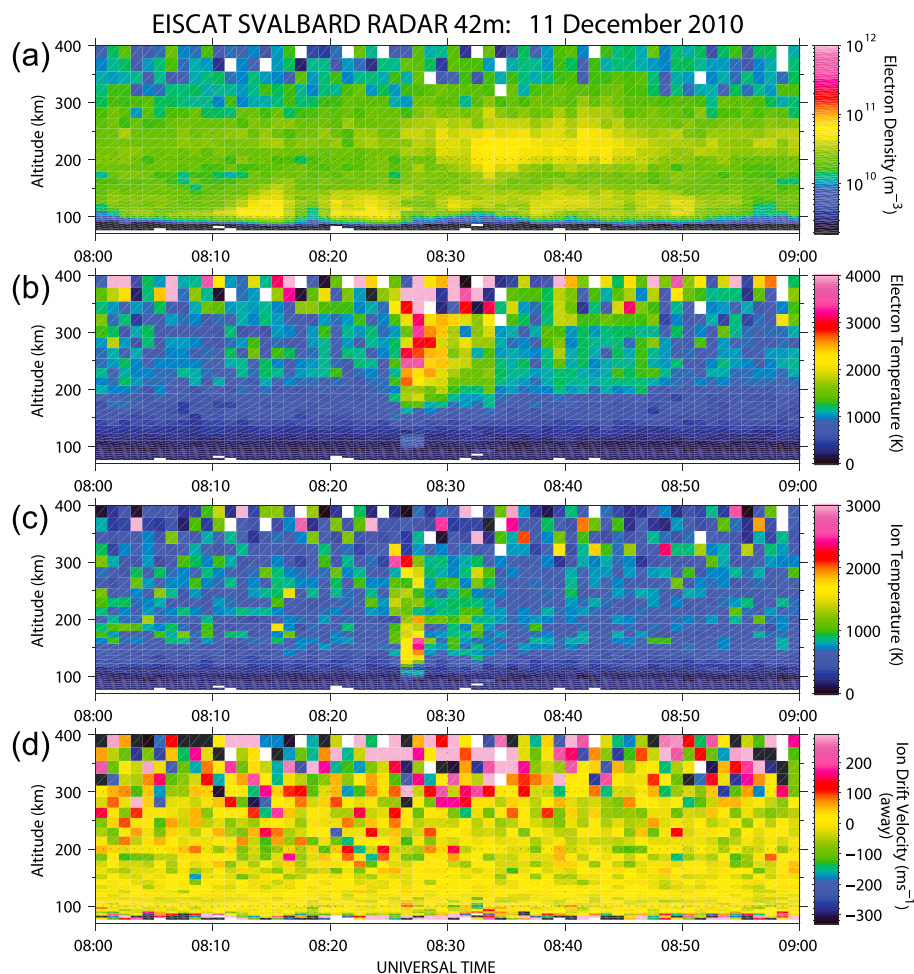
Figure 9. EISCAT Svalbard Radar data of (a) electron density, (b) electron temperature, (c) ion temperature, and (d) vertical ion drift velocity. Transient enhancements of electron and ion temperatures associated with the TCV event were seen, starting at 08:25 UT.

anisotropies in the magnetosphere. The three Svalbard instruments detected the band-limited wave event from 08:30 to 10:00 UT, which follows a broader-band wave burst that occurred between ~08:15 and 08:35 UT. Pc1-frequency wave bursts observed in conjunction with TCVs (or more generally, MIEs) have been reported earlier [e.g., *Arnoldy et al.*, 1988, 1996; *Engebretson et al.*, 2013; *Posch et al.*, 2013]. Data from LOZ display wave activity with a narrower spectral structure that preceded the wave events observed at the Svalbard stations. The LOZ data show increase of the wave frequencies at the onset of the TCV event.

The location of the Pc1 source can be derived from observations of localized precipitation of energetic (>10 keV) protons within the region of anisotropic proton fluxes [e.g., *Yahnin and Yahnina*, 2007]. Figure 6 shows the locations of the four induction-coil magnetometer stations on Svalbard and Russia and the magnetic footprints of low Earth orbit spacecraft that observed such proton precipitation during the EMIC wave event (see the caption in the figure for details). The particle data from the MEPED instrument aboard the NOAA and MetOp spacecraft are presented in Figure 7. The proton precipitation that occurred within the anisotropic zone is marked by pink color. The data show that some localized proton precipitation bursts are consistently seen between 73° and 76° CGM Latitudes. These precipitations have relatively low intensity, and their latitudinal locations significantly vary. Also, they are seen both before and after clear Pc1 observations on Svalbard. Thus, it is doubtful that the precipitation bursts at 73°–76° CGM latitudes indicate the source location of the band-limited Pc1 event.

The spectrograms from the DMSP-F18 spacecraft in Figure 8 show a clear isolated burst of precipitating protons (>10 keV) near 08:30 UT (as encircled in this figure), latitudinally between Svalbard and LOZ (see the
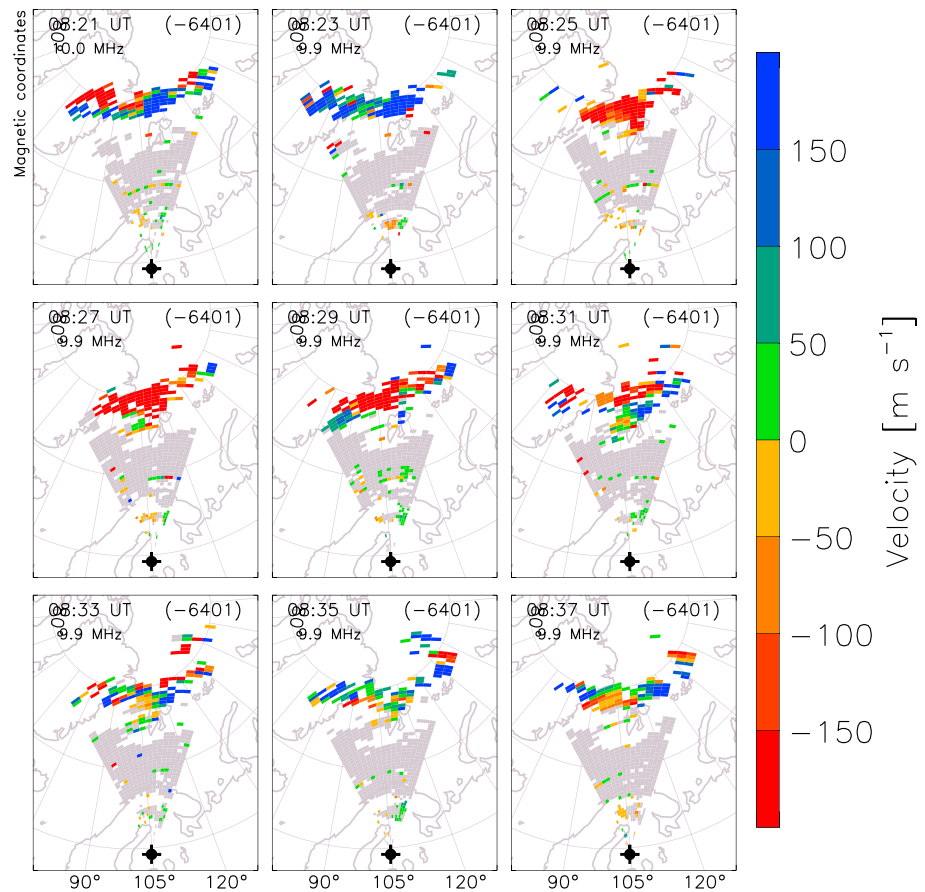
Figure 10. SuperDARN field-of-view scan plots showing convection velocities during the TCV event. Positive velocities indicate equatorward flows (toward the radar) and negative poleward flows (away from the radar).

location of the DMSP spacecraft in Figure 6). A strong proton precipitation burst is seen at nearly the same geographical location in the data from MetOp-2 spacecraft at 09:38 UT (red label in Figure 7). No other low-orbiting spacecraft crossed this geographic location in the time interval of interest. This may mean long-lived localized proton precipitation corotating with the Earth as described by *Frey et al.* [2004]. This is a good source marker for the EMIC wave event in Figure 5.

Disturbances in the ionospheric plasma in association with the TCVs are also observed in EISCAT and Super-DARN data. During the TCVs (from ∼08:20 UT to 08:30 UT), enhancements in electron and ion temperatures starting at ∼08:25 UT were measured by the EISCAT Svalbard Radar, as seen in Figures 9b and 9c. These temperature increases, along with the corresponding electron density increase (Figure 9a), are attributed to soft precipitation associated with the TCVs. No remarkable change in vertical ion drift velocity is observed during the event (Figure 9d).

The FOV scan plot from SuperDARN data (Figure 10) shows ionospheric convection patterns associated with the TCVs. Positive velocities indicate equatorward flows (toward the radar) and negative poleward flows (away from the radar). An abrupt change in convection flows is observed between 08:23 and 08:25 UT, which coincides with the onset of the TCVs. The data near 08:29 and 08:31 UT demonstrate a pattern that is typically seen in twin-cell convection; that is, poleward flows in the central beams and equatorward flows in both the east and west of the beams. These observations are in good agreement with the convection patterns shown in Figure 3. Note that there are no other radar data available during this event, and thus, only FOV velocity maps (line of sight measurements) are presented in this paper.
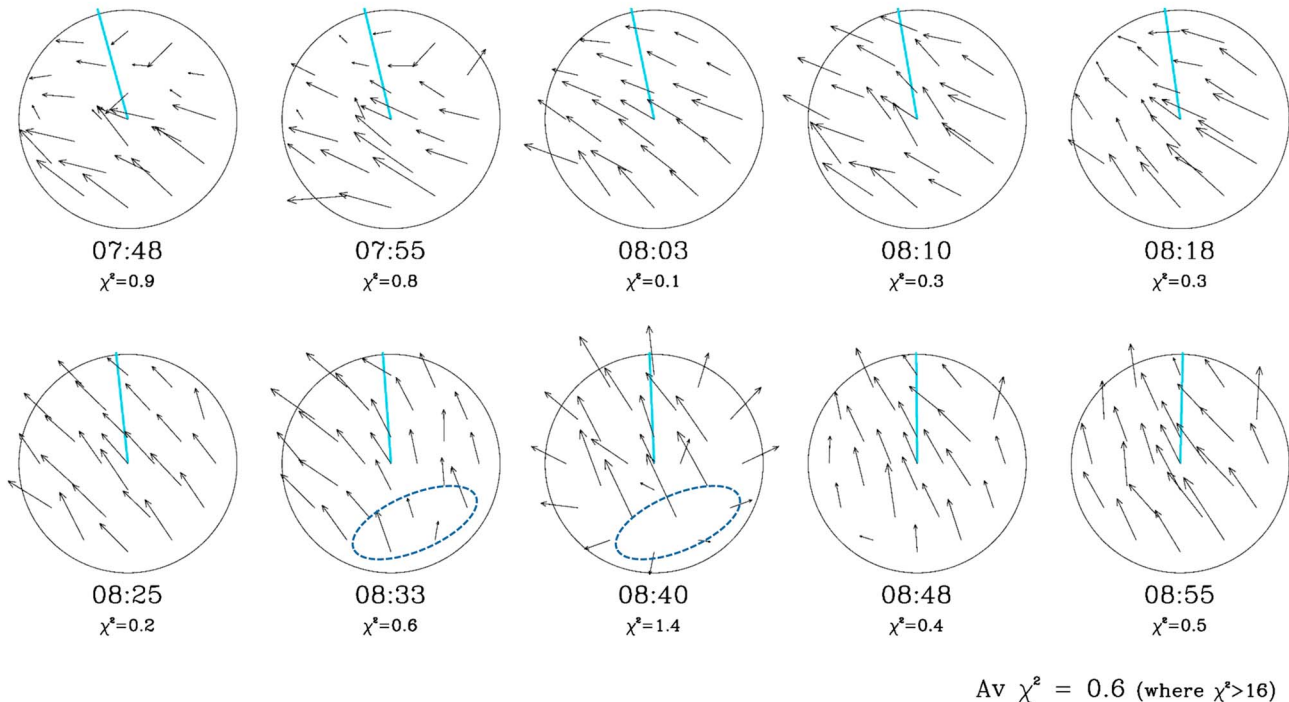
SCANDI wind vectors in Figure 11 showed some structure over the ∼1200 km diameter FOV but were generally smoothly flowing during the first 50 min leading up to the TCV event (07:48–08:33 UT). The upper thermospheric wind speeds (assumed altitude 250 km) were small, with a magnitude around 100 m/s,
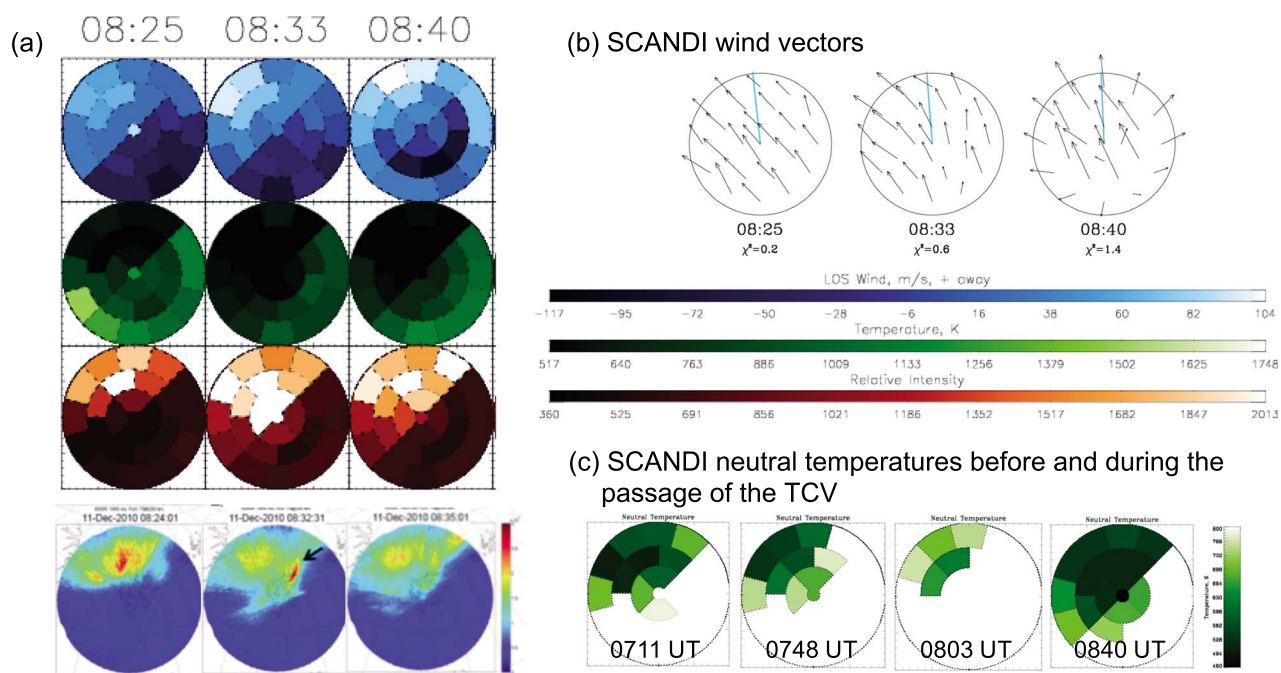
Figure 11. SCANDI observations of neutral winds over LYR. Before the TCV passed, the wind flow was fairly uniform. Beginning near 08:33 UT, winds to the southeast of the station decrease significantly (blue dashed ovals), followed by a clear divergence in the 08:40 UT image (see the vectors around the circle rim), and then a return to a uniform flow by 08:55 UT.

with an error of ±20 to 30 m/s. The error in the wind direction was of the order of $\pm10°$. This smooth neutral wind pattern was disrupted during the passing of the TCV and then began to recover to the original state by the time of the next 7 min exposure. Note that the exposure takes around 7–8 min, including processing time, so each image is a summation of the thermospheric behavior over that period. The time stamp is the end of the exposure. The exposure ending at 08:33 UT showed an apparent reduction in the wind magnitudes in the southeast section of the FOV. By 08:40 UT, a significant divergence was seen in the thermospheric wind flow. By 08:48 UT, the velocities were already returning to a more uniform flow. These small winds are consistent with the quiet conditions seen in the EISCAT Svalbard Radar data in Figure 9. In particular, the ion temperatures were very low (below 800 K), and the field-aligned plasma velocities were hovering around 0 m/s.

The response of the divergence of the neutral winds might be interpreted as a localized upwelling and downwelling response over an FOV of hundreds of kilometers. It is consistent with the current densities shown in Figure 3, which were largest to the north of LYR, and a likely source of Joule heating. The largest magnetometer perturbations (Figure 2) were observed at NAL, which is only around 80 km northwest of LYR and therefore within the first SCANDI ring. To the south, the outermost SCANDI ring covers the region of BJN which showed a much smaller magnetic perturbation than NAL. The disruption of the wind flow at 08:40 UT is consistent with a localized heating source. However, although monostatic determinations of flows are adequate for uniform flows (and have been used regularly with beam-swinging radars), ideally, two or more overlapping FPIs are necessary to characterize unambiguously more complicated wind fields such as shown at 08:40 UT [*Anderson et al.*, 2012].

Figure 12a displays the line-of-sight winds (blue), neutral temperatures (green), and 630.0 nm intensities (red) calculated from the Doppler shifts, Doppler broadening, and peak heights for each of the 25 SCANDI sectors for three exposures ending at 08:25 UT, 08:33 UT, and 08:40 UT. Three of the images from Figure 4 have

Figure 12. (a) SCANDI observations of line-of-sight neutral winds (blue), neutral temperatures (green), and 630.0 nm intensities (red) at 08:25, 08:33, and 0840 UT, with the nearest corresponding all-sky images at the bottom. (b) The SCANDI wind vectors for the same times. (c) The rescaled neutral temperatures to highlight the patch of reduced temperatures in the region of the larger ionospheric currents seen in Figure 3b.

been added at the bottom to show the close correspondence with SCANDI of the spatial distribution of the 630.0 nm intensities. Note that the red line emission during darkness is dominated by dissociative recombination of O^+_2, and so the nighttime intensity is proportional to the electron density (also see the discussion about Figure 4). Figure 12b shows the three corresponding wind vector plots. The SCANDI neutral temperatures were consistent with the EISCAT Svalbard Radar ion temperatures. The ion temperatures directly above LYR were less than 800 K. The SCANDI neutral temperatures showed a greater range over the FOV, varying between 500 and 1100 K. What is interesting is that the neutral temperatures to the northwest were lower than to the southeast rather than the expected consequences of Joule heating. In Figure 12c, the temperature plot was rescaled ($460 - 800$ K) to highlight the spatial structure in the cold northwest sector. The white sectors were temperatures above 800 K. The patch of colder neutral temperatures occurred within a larger-scale temperature structure and general variability in this wide FOV. There is no clear signature in the neutral temperatures that can be attributed purely to the TCV without a modeling study.

4. Discussion and Conclusions

The observations presented in this paper show the telltale signs of TCVs in various data, showing magnetic field deflections, vortical flows, wave events, electron and ion temperature enhancements, and auroral emission and precipitation. The FPI data also show a divergence in the thermospheric winds as the first evidence of coupling to the thermosphere associated with a TCV event, revealing a solar wind-magnetosphere-ionosphere-thermosphere coupling originally generated by a sudden pressure change in the solar wind.

The TCV event presented in this paper occurred simultaneously with a sudden pressure change in the pristine solar wind as observed in OMNI data (Figure 1). Unfortunately, no spacecraft was near the local time and geomagnetic latitude of the event to show transient features near the magnetopause boundary. A number of previous studies, however, attribute generation of TCVs to transient phenomena associated with solar wind dynamic pressure [e.g., *Sibeck et al.*, 1989; *Kivelson and Southwood*, 1991; *Glassmeier and Heppner*, 1992; *Sibeck et al.*, 2003; *Engebretson et al.*, 2013; *Kim et al.*, 2015].

Signatures typically found during TCVs such as bipolar deflections and vortical structures are clearly seen in the magnetometer data as presented in Figures 2 and 3, respectively. Previous TCV studies have reported such signatures using high-latitude ground magnetometer arrays [e.g., *Friis-Christensen et al.*, 1988;

Glassmeier et al., 1989; *Sitar et al.*, 1998; *Engebretson et al.*, 2013; *Kim et al.*, 2015]. The ground equivalent convection patterns inferred from the horizontal components of the magnetometers clearly show the location of the TCV centers at ∼74° CGM latitude. The latitudinal locations of the TCV centers are in good agreement with the previous studies [e.g., *Murr et al.*, 2002; *Zesta et al.*, 2002; *Engebretson et al.*, 2013; *Kim et al.*, 2015]. The ionospheric patterns during TCVs are attributed to the effect of circular Hall currents produced by a pair of oppositely directed FACs. Therefore, the TCV centers indicate the locations of the current systems which map to the magnetospheric boundary deformed due to the transient change in solar wind pressure. *Engebretson et al.* [2013] reported both electron and proton precipitation during a TCV event over Svalbard, the same location where our observations were made.

The coincident TCV location (Figure 3) and intensification of the auroral brightening (Figure 4) indicate that the mechanism that causes the TCV event (likely to be the transient compression of the boundary layer due to the sudden change in solar wind pressure) is also associated with auroral electron precipitation. Auroral emission at 630 nm associated with a TCV event is also reported by *Engebretson et al.* [2013]. The first vortex (the one centered at 08:23 UT as shown in Figure 3) does not appear to produce any clear auroral signature over Svalbard, while the second vortex (08:29 UT) coincides well with the auroral patch brightening commencing at 8:28 UT. The Pc1 waves simultaneously observed during the TCV event (Figure 5) suggest the link between the TCVs and auroral precipitation in association with transient compression of the magnetosphere. *Engebretson et al.* [2013] also observed Pc1 waves associated with a TCV event and auroral precipitation, suggesting that such waves are stimulated by the rapid, transient compression of a marginally unstable pitch angle distribution of energetic ions in the outer magnetosphere. Compression-associated EMIC waves have also been reported in a number of studies [e.g., *Engebretson et al.*, 2002; *Usanova et al.*, 2008, 2010, 2012; *Clausen et al.*, 2011].

Given the limited information (mostly due to lack of adequate space-ground conjunction observations of the wave), it is difficult to argue that the entire wave activity shown in Figure 5 is associated with the TCV event. Obviously, the Pc1 burst which occurred between 08:15 and 08:35 UT appears to be closely related to the solar wind pressure pulse (Figure 1) and thus the TCVs. The top three panels in Figure 5 display data from the UNH induction-coil magnetometer network on Svalbard, whereas the bottom panel shows data from LOZ, which is along a similar magnetic meridian but at a much lower latitude than the UNH ones (see Table 1). The LOZ data suggest that the enhancement of spectral power and gradual increase of the wave frequency (from 08:00 to 08:30 UT) appear to be correlated with the magnetospheric compression indicated by the $SYM - H$ index as shown in Figure 1. Thus, one can argue that the longer-lasting EMIC wave activity (from 07:00 to 10:00 UT) might be associated with global magnetospheric dynamics rather than the transient event. The UNH and LOZ magnetometers are not intercalibrated, and thus, the spectral power between the two types (NAL, LYR, HOR versus LOZ) should not be directly compared. Nevertheless, the overall spectral and temporal structures from LOZ data are much clearer than those from other stations. In addition, the LOZ data are compared with the data from Barentsburg (BAB) on Svalbard, which is situated close to LYR and where another magnetometer identical to that in LOZ is operated by Polar Geophysical Institute. The spectrogram from BAB (not presented here) shows the same signal structure as seen in the spectrograms from the UNH stations, and this signal is weaker than that in LOZ, indicating that the source of the entire wave event is closer to LOZ. This agrees with localization of the EMIC wave source using observations of precipitating protons. On the contrary, the lack of the Pc1 burst in LOZ data supports the idea that the burst is associated with the TCVs seen over Svalbard.

It should also be noted that waves that enter the ionosphere propagate horizontally in the ionospheric waveguide (duct) [e.g., *Kim et al.*, 2011], making it challenging to estimate the wave source region. Measurements of precipitating particle flux are often used to locate the source. The isolated burst of precipitating protons shown in Figure 8 can be used as a proxy wave source marker. Such a latitudinally localized EMIC wave source region has been suggested by *Frey et al.* [2004] and *Yahnin and Yahnina* [2007] on the basis of proton aurora patches and Pc1 observations. We suggest that the wave source might be well within the magnetosphere, while the TCV center is mapped to the region at or near the magnetopause. A pressure pulse at the magnetopause generates a compressional wave, which propagates across field lines through the magnetosphere, and thus, shear Alfvén waves form via a mode conversion [e.g., *Lysak and Lee*, 1992]. This process can provide energy to generate EMIC waves. An in-depth study regarding the relationship between TCVs and EMIC wave generation is left for a future study.

We use SCANDI to measure thermospheric temperature and wind to study ion-neutral coupling during the TCVs. One of the outstanding questions regarding the occurrence of TCVs is how the current systems such as FACs and Hall currents are linked with the neutrals in the thermosphere. The Hall current patterns shown in Figure 3 associated with the TCVs and the resulting FACs appear to coincide with the divergence of the neutrals as shown in Figure 11.

The EISCAT Svalbard Radar measured enhanced electron and ion temperatures, consistent with particle precipitation and enhanced Joule heating, in association with the transient event (Figure 9). The upper panel in the same figure also shows small enhancement of the electron density from 08:10 to 08:51 UT in the *E* region and from 08:30 to 08:45 UT in the *F* region. The *F* region enhancement appears to be associated with the transient event. However, the electron densities are generally low, consistent with solar minimum.

Particle precipitation along the field lines leads to enhancement of ionospheric conductivity [e.g., *Zhu et al.*, 1997; *Engebretson et al.*, 2013]. Energy deposition from the ionosphere to thermosphere, which results in Joule heating, can provide energy to modify or accelerate neutral winds. *Aruliah and Griffin* [2001] compared FPI observations of thermospheric neutral winds and EISCAT radar observations of ionospheric plasma convection over Northern Scandinavia, suggesting that the neutral atmosphere is capable of responding to ionospheric changes in spatial and temporal scale sizes of less than a few hundred kilometers and tens of minutes, respectively. *Lu et al.* [1995] found that although the majority of the magnetospheric electromagnetic energy dissipated in the high-latitude ionosphere is converted into Joule heating, only a small fraction of it goes to mechanical energy to accelerate thermospheric neutral winds. The relationship is not quantitatively examined in our study. Besides the physical link, it is not clear what the scale size of the neutral wind disturbance is in relation to the spatial extent of the Hall current system produced by the transient event. In fact, observations show that the scale size of TCV events is approximately in the range of a few thousand kilometers [e.g., *Glassmeier et al.*, 1989; *Glassmeier and Heppner*, 1992; *Zesta et al.*, 1999; *Amm et al.*, 2002; *Murr et al.*, 2002; *Kim et al.*, 2015]. Therefore, it is necessary to examine how much energy is required to provide energy for neutral winds given the spatial extent of the ionospheric disturbance due to the associated particle precipitation during TCVs. This task is left for future work.

TCVs are the result of solar wind energy transfer to the magnetosphere, ionosphere, and thermosphere. During TCVs, large-scale FACs couple to the ionosphere, producing aurora, ionospheric convection change, and ionospheric and thermospheric heating. The main conclusions of the paper are as follows:

1. TCVs were observed that passed directly over LYR and through the EISCAT Svalbard Radar beam, as well as the all-sky camera field of view. Brief but clear heating was observed in the EISCAT data.
2. Induction-coil magnetometers show the onset of EMIC waves at the approximate time of the TCV event driven by a pressure pulse in the solar wind. This implies that they were generated by increased temperature anisotropies resulting from a compression on the dayside magnetosphere.
3. SuperDARN flows show direct observations of vortical flows.
4. SCANDI data show a divergence in thermospheric winds during the TCVs, presumably due to thermospheric heating associated with the current closure linked to FACs generated by the TCVs.
5. This is the first-ever observations showing that solar wind pressure impulse-related transient phenomena can affect even the upper atmospheric dynamics via current systems established by a magnetosphere-ionosphere-thermosphere coupling process.

References

Amm, O., M. J. Engebretson, T. Hughes, L. Newitt, A. Viljanen, and J. Watermann (2002), A traveling convection vortex event study: Instantaneous ionospheric equivalent currents, estimation of field-aligned currents, and the role of induced currents, *J. Geophys. Res.*, *107*(A11), 1334, doi:10.1029/2002JA009472.

Anderson, B. J., R. E. Erlandson, and L. J. Zanetti (1992), A statistical study of Pc 1–2 magnetic pulsations in the equatorial magnetosphere. 1. Equatorial occurrence distributions, *J. Geophys. Res.*, *97*, 3075–3088, doi:10.1029/91JA02706.

Araki, T. (1977), Global structure of geomagnetic sudden commencements, *Planet. Space Sci.*, *25*, 373–384, doi:10.1016/0032-0633(77)90053-8.

Araki, T. (1994), A physical model of the geomagnetic sudden commencement, in *Solar Wind Sources of Magnetospheric Ultra-Low-Frequency Waves, Geophys. Monogr. Ser.*, vol. 81, edited by M. J. Engebreston, K. Takahashi, and M. Scholer, pp. 183–200, AGU, Washington, D. C., doi:10.1029/GM081p0183.

Arnoldy, R. L., M. J. Engebretson, and L. J. Cahill Jr. (1988), Bursts of Pc 1-2 near the ionospheric footprint of the cusp and their relationship to flux transfer events, *J. Geophys. Res.*, *93*, 1007–1016, doi:10.1029/JA093iA02p01007.

Arnoldy, R. L., M. J. Engebretson, J. L. Alford, R. E. Erlandson, and B. J. Anderson (1996), Magnetic impulse events and associated Pc 1 bursts at dayside high latitudes, *J. Geophys. Res.*, *101*, 7793–7800, doi:10.1029/95JA03378.

Aruliah, A. L., and E. Griffin (2001), Evidence of meso-scale structure in the high-latitude thermosphere, *Ann. Geophys.*, *19*, 37–46, doi:10.5194/angeo-19-37-2001.

Aruliah, A. L., D. Rees, and T. J. Fuller-Rowell (1991), The combined effect of solar and geomagnetic activity on high latitude thermospheric neutral winds. I-Observations, *J. Atmos. Terr. Phys.*, *53*, 467–483.

Aruliah, A. L., E. M. Griffin, H.-C. I. Yiu, I. McWhirter, and A. Charalambous (2010), SCANDI—An all-sky Doppler imager for studies of thermospheric spatial structure, *Ann. Geophys.*, *28*, 549–567, doi:10.5194/angeo-28-549-2010.

Clauer, C. R. (2003), Ionospheric observations of waves at the inner edge of the low latitude boundary layer, in *Earth's Low Latitude Boundary Layer*, vol. 133, edited by P. Newell and T. Onsager, pp. 297–309, AGU, Washington, D. C., doi:10.1029/133GM30

Clauer, C. R., and V. G. Petrov (2002), A statistical investigation of traveling convection vortices observed by the west coast Greenland magnetometer chain, *J. Geophys. Res.*, *107*(A7), 1148, doi:10.1029/2001JA000228.

Clauer, C. R., and A. J. Ridley (1995), Ionospheric observations of magnetospheric low-latitude boundary layer waves on August 4, 1991, *J. Geophys. Res.*, *100*, 21,873–21,884, doi:10.1029/95JA00678.

Clausen, L. B. N., J. B. H. Baker, J. M. Ruohoniemi, and H. J. Singer (2011), EMIC waves observed at geosynchronous orbit during solar minimum: Statistics and excitation, *J. Geophys. Res.*, *116*, A10205, doi:10.1029/2011JA016823.

Dougal, E. R., K. Nykyri, and T. W. Moore (2013), Mapping of the quasi-periodic oscillations at the flank magnetopause into the ionosphere, *Ann. Geophys.*, *31*, 1993–2011, doi:10.5194/angeo-31-1993-2013.

Engebretson, M. J., W. K. Peterson, J. L. Posch, M. R. Klatt, B. J. Anderson, C. T. Russell, H. J. Singer, R. L. Arnoldy, and H. Fukunishi (2002), Observations of two types of Pc 1–2 pulsations in the outer dayside magnetosphere, *J. Geophys. Res.*, *107*(A11), 1451, doi:10.1029/2001JA000198.

Engebretson, M. J., et al. (2013), Multi-instrument observations from Svalbard of a traveling convection vortex, electromagnetic ion cyclotron wave burst, and proton precipitation associated with a bow shock instability, *J. Geophys. Res. Space Physics*, *118*, 2975–2997, doi:10.1002/jgra.50291.

Fillingim, M. O., J. P. Eastwood, G. K. Parks, V. Angelopoulos, I. R. Mann, S. B. Mende, and A. T. Weatherwax (2011), Polar UVI and THEMIS GMAG observations of the ionospheric response to a hot flow anomaly, *J. Atmos. Sol. Terr. Phys.*, *73*, 137–145, doi:10.1016/j.jastp.2010.03.001.

Frey, H. U., G. Haerendel, S. B. Mende, W. T. Forrester, T. J. Immel, and N. ØStgaard (2004), Subauroral morning proton spots (SAMPS) as a result of plasmapause-ring-current interaction, *J. Geophys. Res.*, *109*, A10305, doi:10.1029/2004JA010516.

Friis-Christensen, E., S. Vennerstrom, M. A. McHenry, and C. R. Clauer (1988), Ionospheric traveling convection vortices observed near the polar cleft—A triggered response to sudden changes in the solar wind, *Geophys. Res. Lett.*, *15*, 253–256, doi:10.1029/GL015i003p00253.

Glassmeier, K.-H., and C. Heppner (1992), Traveling magnetospheric convection twin vortices—Another case study, global characteristics, and a model, *J. Geophys. Res.*, *97*, 3977–3992, doi:10.1029/91JA02464.

Glassmeier, K.-H., M. Hoenisch, and J. Untiedt (1989), Ground-based and satellite observations of traveling magnetospheric convection twin vortices, *J. Geophys. Res.*, *94*, 2520–2528, doi:10.1029/JA094iA03p02520.

Goertz, C. K., E. Nielsen, A. Korth, C. Haldoupis, P. Hoeg, D. Hayward, and K. H. Glassmeier (1985), Observations of a possible ground signature of flux transfer events, *J. Geophys. Res.*, *90*, 4069–4078, doi:10.1029/JA090iA05p04069.

Kataoka, R., H. Fukunishi, and L. J. Lanzerotti (2003), Statistical identification of solar wind origins of magnetic impulse events, *J. Geophys. Res.*, *108*(A12), 1436, doi:10.1029/2003JA010202.

Kataoka, R., H. Fukunishi, S. Fujita, T. Tanaka, and M. Itonaga (2004), Transient response of the Earth's magnetosphere to a localized density pulse in the solar wind: Simulation of traveling convection vortices, *J. Geophys. Res.*, *109*, A03204, doi:10.1029/2003JA010287.

Kim, H., M. R. Lessard, M. J. Engebretson, and M. A. Young (2011), Statistical study of Pc1–2 wave propagation characteristics in the high-latitude ionospheric waveguide, *J. Geophys. Res.*, *116*, A07227, doi:10.1029/2010JA016355.

Kim, H., C. R. Clauer, M. J. Engebretson, J. Matzka, D. G. Sibeck, H. J. Singer, C. Stolle, D. R. Weimer, and Z. Xu (2015), Conjugate observations of traveling convection vortices associated with transient events at the magnetopause, *J. Geophys. Res. Space Physics*, *120*, 2015–2035, doi:10.1002/2014JA020743.

Kivelson, M. G., and D. J. Southwood (1991), Ionospheric traveling vortex generation by solar wind buffeting of the magnetosphere, *J. Geophys. Res.*, *96*, 1661–1667, doi:10.1029/90JA01805.

Lanchester, B. S., M. H. Rees, D. Lummerzheim, A. Otto, K. J. F. Sedgemore-Schulthess, H. Zhu, and I. W. McCrea (2001), Ohmic heating as evidence for strong field-aligned currents in filamentary aurora, *J. Geophys. Res.*, *106*, 1785–1794, doi:10.1029/1999JA000292.

Lanzerotti, L. J., A. Wolfe, C. G. Maclennan, L. V. Medford, and R. D. Hunsucker (1987), Ionosphere and ground-based response to field-aligned currents near the magnetospheric cusp regions, *J. Geophys. Res.*, *92*, 7739–7743, doi:10.1029/JA092iA07p07739.

Lu, G., A. D. Richmond, B. A. Emery, and R. G. Roble (1995), Magnetosphere-ionosphere-thermosphere coupling: Effect of neutral winds on energy transfer and field-aligned current, *J. Geophys. Res.*, *100*, 19,643–19,660, doi:10.1029/95JA00766.

Lühr, H., M. Lockwood, P. E. Sandholt, T. L. Hansen, and T. Moretto (1996), Multi-instrument ground-based observations of a travelling convection vortices event, *Ann. Geophys.*, *14*, 162–181, doi:10.1007/s00585-996-0162-z.

Lühr, H., M. Rother, W. Köhler, P. Ritter, and L. Grunwaldt (2004), Thermospheric up-welling in the cusp region: Evidence from CHAMP observations, *Geophys. Res. Lett.*, *31*, L06805, doi:10.1029/2003GL019314.

Lysak, R. L., and D.-H. Lee (1992), Response of the dipole magnetosphere to pressure pulses, *Geophys. Res. Lett.*, *19*, 937–940, doi:10.1029/92GL00625.

McHenry, M. A., and C. R. Clauer (1987), Modeled ground magnetic signatures of flux transfer events, *J. Geophys. Res.*, *92*, 11,231–11,240, doi:10.1029/JA092iA10p11231.

McHenry, M. A., C. R. Clauer, E. Friis-Christensen, P. T. Newell, and J. D. Kelly (1990), Ground observations of magnetospheric boundary layer phenomena, *J. Geophys. Res.*, *95*, 14,995–15,005, doi:10.1029/JA095iA09p14995.

Moretto, T., and A. Yahnin (1998), Mapping travelling convection vortex events with respect to energetic particle boundaries, *Ann. Geophys.*, *16*, 891–899, doi:10.1007/s00585-998-0891-2.

Moretto, T., M. Hesse, A. Yahnin, A. Ieda, D. Murr, and J. F. Watermann (2002), Magnetospheric signature of an ionospheric traveling convection vortex event, *J. Geophys. Res.*, *107*(A6), 1072, doi:10.1029/2001JA000049.

Murr, D. L., and W. J. Hughes (2003), Solar wind drivers of traveling convection vortices, *Geophys. Res. Lett.*, *30*(7), 1354, doi:10.1029/2002GL015498.

Murr, D. L., W. J. Hughes, A. S. Rodger, E. Zesta, H. U. Frey, and A. T. Weatherwax (2002), Conjugate observations of traveling convection vortices: The field-aligned current system, *J. Geophys. Res.*, *107*(A10), 1306, doi:10.1029/2002JA009456.

Otto, A., D. Lummerzheim, H. Zhu, Ø. Lie-Svendsen, M. H. Rees, and B. S. Lanchester (2003), Excitation of tall auroral rays by ohmic heating in field-aligned current filaments at F region heights, *J. Geophys. Res.*, *108*(A4), 8017, doi:10.1029/2002JA009423.

Posch, J. L., M. J. Engebretson, A. J. Witte, D. L. Murr, M. R. Lessard, M. G. Johnsen, H. J. Singer, and M. D. Hartinger (2013), Simultaneous traveling convection vortex events and Pc1 wave bursts at cusp latitudes observed in Arctic Canada and Svalbard, *J. Geophys. Res. Space Physics*, *118*, 6352–6363, doi:10.1002/jgra.50604.

Sibeck, D. G., R. E. Lopez, and W. Baumjohann (1989), Solar wind dynamic pressure variations and transient magnetospheric signatures, *Geophys. Res. Lett.*, *16*, 13–16, doi:10.1029/GL016i001p00013.

Sibeck, D. G., N. B. Trivedi, E. Zesta, R. B. Decker, H. J. Singer, A. Szabo, H. Tachihara, and J. Watermann (2003), Pressure-pulse interaction with the magnetosphere and ionosphere, *J. Geophys. Res.*, *108*(A2), 1095, doi:10.1029/2002JA009675.

Sitar, R. J., J. B. Baker, C. R. Clauer, A. J. Ridley, J. A. Cumnock, V. O. Papitashvili, J. Spann, M. J. Brittnacher, and G. K. Parks (1998), Multi-instrument analysis of the ionospheric signatures of a hot flow anomaly occurring on July 24, 1996, *J. Geophys. Res.*, *23*, 103,357–23,372, doi:10.1029/98JA01916.

Thayer, J. P., and J. Semeter (2004), The convergence of magnetospheric energy flux in the polar atmosphere, *J. Atmos. Sol. Terr. Phys.*, *66*, 807–824, doi:10.1016/j.jastp.2004.01.035.

Tian, A. M., X. C. Shen, Q. Q. Shi, B. B. Tang, M. Nowada, Q. G. Zong, and S. Y. Fu (2016), Dayside magnetospheric and ionospheric responses to solar wind pressure increase: Multispacecraft and ground observations, *J. Geophys. Res. Space Physics*, *121*, 10,813–10,830, doi:10.1002/2016JA022459.

Usanova, M. E., I. R. Mann, I. J. Rae, Z. C. Kale, V. Angelopoulos, J. W. Bonnell, K.-H. Glassmeier, H. U. Auster, and H. J. Singer (2008), Multipoint observations of magnetospheric compression-related EMIC Pc1 waves by THEMIS and CARISMA, *Geophys. Res. Lett.*, *35*, L17S25, doi:10.1029/2008GL034458.

Usanova, M. E., et al. (2010), Conjugate ground and multisatellite observations of compression-related EMIC Pc1 waves and associated proton precipitation, *J. Geophys. Res.*, *115*, A07208, doi:10.1029/2009JA014935.

Usanova, M. E., I. R. Mann, J. Bortnik, L. Shao, and V. Angelopoulos (2012), THEMIS observations of electromagnetic ion cyclotron wave occurrence: Dependence on AE, SYM-H, and solar wind dynamic pressure, *J. Geophys. Res.*, *117*, A10218, doi:10.1029/2012JA018049.

Valladares, C. E., D. Alcaydé, J. V. Rodriguez, J. M. Ruohoniemi, and A. P. van Eyken (1999), Observations of plasma density structures in association with the passage of traveling convection vortices and the occurrence of large plasma jets, *Ann. Geophys.*, *17*, 1020–1039, doi:10.1007/s00585-999-1020-6.

Wang, H., H. Lühr, A. Ridley, and T. Huang (2014), The spatial distribution of region 2 field-aligned currents relative to subauroral polarization stream, *Ann. Geophys.*, *32*, 533–542, doi:10.5194/angeo-32-533-2014.

Wang, W., M. Wiltberger, A. G. Burns, S. C. Solomon, T. L. Killeen, N. Maruyama, and J. G. Lyon (2004), Initial results from the coupled magnetosphere-ionosphere-thermosphere model: Thermosphere-ionosphere responses, *J. Atmos. Sol. Terr. Phys.*, *66*, 1425–1441, doi:10.1016/j.jastp.2004.04.008.

Wiltberger, M., W. Wang, A. G. Burns, S. C. Solomon, J. G. Lyon, and C. C. Goodrich (2004), Initial results from the coupled magnetosphere ionosphere thermosphere model: Magnetospheric and ionospheric responses, *J. Atmos. Sol. Terr. Phys.*, *66*, 1411–1423, doi:10.1016/j.jastp.2004.03.026.

Yahnin, A., and T. Yahnina (2007), Energetic proton precipitation related to ion cyclotron waves, *J. Atmos. Sol. Terr. Phys.*, *69*, 1690–1706, doi:10.1016/j.jastp.2007.02.010.

Yahnin, A., E. Titova, A. Lubchich, T. Bosinger, J. Manninen, T. Turunen, T. Hansen, O. Troshichev, and A. Kotikov (1995), Dayside high latitude magnetic impulsive events: Their characteristics and relationship to sudden impulses, *J. Atmos. Terr. Phys.*, *57*, 1569–1582, doi:10.1016/0021-9169(95)00090-O.

Yahnin, A. G., V. G. Vorobjev, T. Bösinger, R. Rasinkangas, D. G. Sibeck, and P. T. Newell (1997), On the source region of traveling convection vortices, *Geophys. Res. Lett.*, *24*, 237–240, doi:10.1029/96GL03969.

Zesta, E., W. J. Hughes, M. J. Engebretson, T. J. Hughes, A. J. Lazarus, and K. I. Paularena (1999), The November 9, 1993, traveling convection vortex event: A case study, *J. Geophys. Res.*, *104*, 28,041–28,058, doi:10.1029/1999JA900306.

Zesta, E., W. J. Hughes, and M. J. Engebretson (2002), A statistical study of traveling convection vortices using the Magnetometer Array for Cusp and Cleft Studies, *J. Geophys. Res.*, *107*(A10), 1317, doi:10.1029/1999JA000386.

Zhu, L., P. Gifford, J. J. Sojka, and R. W. Schunk (1997), Model study of ground magnetic signatures of traveling convection vortices, *J. Geophys. Res.*, *102*, 7449–7460, doi:10.1029/96JA03682.